

PAPER • OPEN ACCESS

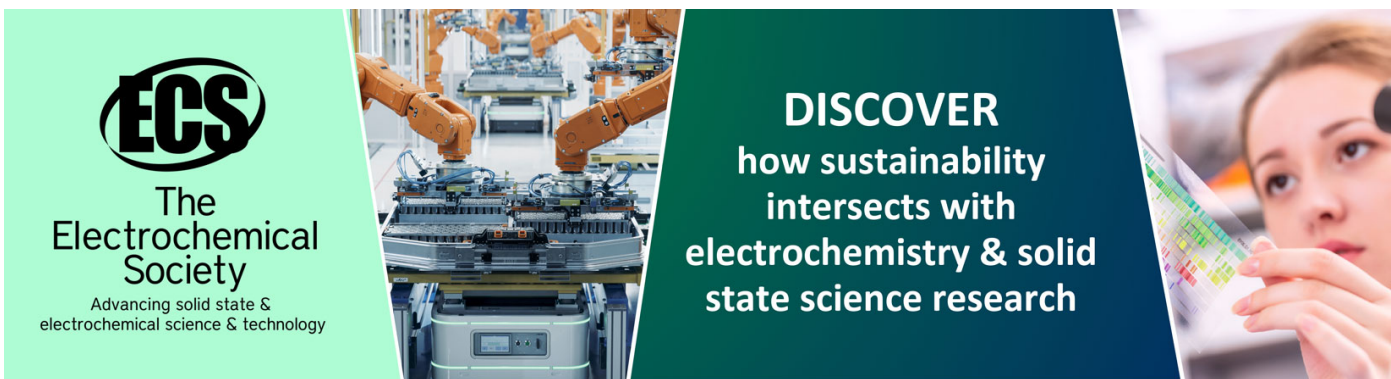
Aerodynamic Study of Low-Speed Wind Tunnel Contraction Section: Design and Manufacturing

To cite this article: Alaa A Kareem *et al* 2021 *IOP Conf. Ser.: Mater. Sci. Eng.* **1094** 012077

View the [article online](#) for updates and enhancements.

You may also like

- [Numerical simulation of tsunami propagation with Finite Difference Method and Runge Kutta 4th Order Method \(study case : south coast of Java island\)](#)
Firdaus Priyatno Putra, Shaffiani Nurul Fajar, Prima Aditya et al.
- [Numerical Solution of Volterra Integro-Differential Equation Using 6th Order Runge-Kutta Method](#)
A. F. Al-Shimmary, A. K. Hussain and S.K. Radhi
- [On The Solution And Stability Analysis Of 6th order Bvp By Special Multistep Methods](#)
C Balarama Krishna, G Anusha, R Archana Reddy et al.



ECS
The
Electrochemical
Society
Advancing solid state &
electrochemical science & technology

DISCOVER
how sustainability
intersects with
electrochemistry & solid
state science research

Aerodynamic Study of Low- Speed Wind Tunnel Contraction Section: Design and Manufacturing

Alaa A Kareem, Mohamad K Abbas and Farhan A Khammas

Al-Nahrain University, College of Engineering, Mechanical Engineering Department, Baghdad, Iraq

E-mail: alaa.kareem@uokufa.edu.iq

Abstract. This work aims to improve the visualization of a subsonic open section type smoke tunnel, which already exists in the AL-Nahrain University/ College of Engineering /Mechanical Department Laboratory. This study focuses on modifying the contraction section only to improve the airflow properties in the test section. A numerical study with ANSYS FLUENT R19.0 was carried out to characterize the flow via the contraction section. The parameters that are suggested to be modified are the wall profile and the length of the contraction section. The analysis includes the original contraction section and suggested new profiles to be compared under the same boundary conditions. The new suggested profiles for this work are polynomials of orders (6th, 7th, 8th, 9th, and 10th). A unique analysis is achieved for the 9th order profile, where it is tested with four different inflection points (0.5L, 0.55L, 0.6L, and 0.65L). The study focuses on the uniformity, turbulence intensity, boundary layer thickness at the contraction section exit plain, beside the boundary layer separation along with the contraction as comparing parameters. Experimental work was done to validate the numerical results. The experiment work includes building a half-scale of the original smoke tunnel to monitor the new contraction's direct influence on the test section's flow. The result showed that the 9th-order wall profile with an inflection point at 0.65L and length of 0.93m is the best contraction for the aimed smoke tunnel.

Keywords. Aerodynamic, Wind tunnel, ANSYS FLUENT.

1. Introduction

The tunnels are one of the most critical test devices in the field of fluids. The engineering applications with high accuracy and impressive performance, such as ships, submarines, aircraft, missiles, vehicles, and many other applications that deal with fluids, have been developed with this device's help. In aerodynamics, the tunnels usually use air as a working fluid, so that it is known as (wind tunnels). The wind tunnels' primary purpose is to simulate the wind flow around bodies to study the effect of wind on models by measuring the exerted forces. Sometimes these wind tunnels are equipped with a smoke generator to visualize the airflow pattern around the objects. Visualizing the flow forms is one of the essential tools for designers and researchers. The physical phenomena that happen to run during objects' passage are visible, thus facilitating appropriate mathematical models and improving designs according to flow patterns. The vital part of almost all wind or smoke tunnels is the contraction section and is therefore of great interest to researchers and designers. This section gained its importance through its direct influence on the flow's properties inside the test section. Furthermore, it is responsible for the performance accuracy of the most important testing device in aerodynamics. The



contraction's primary vital purposes are highly increasing the mean velocity, which reduces the power required for running the tunnel. Reducing the pressure in the settling chamber, which causes to reduce pressure losses accrued by the screens and honeycomb; hence the power factor of the tunnel will be reduced. Decreasing both the fluctuated and mean velocities to a smaller fraction of the average velocity at a particular cross-section area, reducing the turbulent intensity in the streamwise direction by spreading the vortex's filaments in the direction of the flow and compressing the filaments that have a perpendicular axis to the streamwise direction. Several papers on the selection of contraction ratio and wall shape and measuring performance have been published over the decades. The general rules for designing a contraction section are that it should produce a uniform and steady stream and require the avoidance of flow separation. The contraction length should be as minimum as possible and gives a minimum thickness of the boundary layer at the exit plane. The non-uniformities at the exit must equal to the maximum tolerable for a given application (typically 0.5% outside the boundary layer). Large contraction ratios are advantageous, but that means higher construction and running costs besides the possible problem of noise and separation near the end. Therefore, a contraction ratio in the range of (9-6) is usually used. See R.D. Mehta and P. Bradshaw [1]. The performance of small, low-speed contraction with a maximum of 40 m/s and test section below 0.5 m², including calculating the wall pressure distribution and wall velocity distribution prediction, is suggested as a procedure using a three-dimensional potential flow method although a panel method. This method was used to investigate for profiles: 3rd-order, 5th-order, 7th-order, and matched cubic profile. This investigation shows that the 5th-order profile is the one that satisfies most criteria of the required contraction. See James H. Bell and Rabindra D. Mehta [2]. According to the mentioned criteria, many suggested contraction profiles were investigated to improve a specific tunnel's performance. A study of two matched curves with a mathematical models designed to have variable power n, this study show that a higher power values produce higher uniformity. See Yao-xi Su [3]. A numerical and experimental study for flow characteristics in a contracting with square inlet and outlet with a contraction ratio of 9, and matched cubic curve profile achieved by Fuh-Min Fang et al. [4]. Many designs have been proposed, studied, and compared to improve the performance of a particular tunnel basing on different criteria according to the operational purpose of the aimed tunnel see references [5-22]. It is worth mentioning here that there is no optimum design suitable for all tunnel types. Many profiles are reinvestigated for other tunnels in the same category with different operational conditions. A numerical and experimental study was achieved to improve the contraction section performance focusing on the contraction wall profile and length.

2. Mathematical models formulation

The primary mathematical model for the new suggested profile is shown in Table 1. The first profile represents the mathematical model of the original contraction section.

Table 1. Primary suggested mathematical models.

1	$h = [-10\xi^3 + 15\xi^4 - 6\xi^5](H_i - H_o) + H_i$
2	$y = ax^6 + bx^5 + cx^4 + dx^3 + ex^2 + fx + g$
3	$y = ax^7 + bx^6 + cx^5 + dx^4 + ex^3 + fx^2 + gx + k$
4	$y = ax^8 + bx^7 + cx^6 + dx^5 + ex^4 + fx^3 + gx^2 + kx + m$
5	$y = ax^9 + bx^8 + cx^7 + dx^6 + ex^5 + fx^4 + gx^3 + kx^2 + mx + n$
6	$y = ax^{10} + bx^9 + cx^8 + dx^7 + ex^6 + fx^5 + gx^4 + kx^3 + mx^2 + nx + p$

Table 1 ($\xi=x/L$), where L is the contraction length, H_i and H_o are the contraction inlet and exit heights, respectively, for the 5th-order equation, and it could be used directly by specifying the required contraction length. The rest of the equation should solve according to a geometrical boundary condition. Table 2 shows an example of the boundary conditions needed to solve the 10th-order polynomial showed in Table 1. Applying the boundary condition will be resulting in equations with several unknown coefficients, which is needed to be determined. The matrix A and vectors x and B 1-3 can be used to calculate the values of these coefficients according to Equation 4.

Table 2. Boundary conditions for solving the 10th order polynomial.

At the Inlet	At the Turning point	At the exit
$y_{(0)} = H$		$y_{(L)} = h$
$\frac{d}{dx}y_{(0)} = 0$	$\frac{d^2}{dx^2}y_{(x_i)} = 0$	$\frac{d}{dx}y_{(L)} = 0$
$\frac{d^2}{dx^2}y_{(0)} = 0$		$\frac{d^2}{dx^2}y_{(L)} = 0$
$\frac{d^3}{dx^3}y_{(0)} = 0$		$\frac{d^3}{dx^3}y_{(L)} = 0$
$\frac{d^4}{dx^4}y_{(0)} = 0$		$\frac{d^4}{dx^4}y_{(L)} = 0$

$$A = \begin{bmatrix} 90x_i^8 & 72x_i^7 & 56x_i^6 & 42x_i^5 & 30x_i^4 & 20x_i^3 \\ L^{10} & L^9 & L^8 & L^7 & L^6 & L^5 \\ 10L^9 & 9L^8 & 8L^7 & 7L^6 & 6L^5 & 5L^4 \\ 90L^8 & 72L^7 & 56L^6 & 42L^5 & 30L^4 & 20L^3 \\ 720L^7 & 504L^6 & 336L^5 & 210L^4 & 120L^3 & 60L^2 \\ 5040L^6 & 3024L^5 & 1680L^4 & 840L^3 & 360L^2 & 120L \end{bmatrix} \tag{1}$$

$$x = \begin{bmatrix} a \\ b \\ c \\ d \\ e \\ f \end{bmatrix} \tag{2}$$

$$B = \begin{bmatrix} 0 \\ h - H \\ 0 \\ 0 \\ 0 \\ 0 \end{bmatrix} \tag{3}$$

$$x = (A^{-1}) * B \tag{4}$$

This work will investigate the suggested profiles with two different lengths, which is mean a change in one of the geometrical boundary conditions so that the mathematical models should be solved twice to get two different lengths for each profile. The coefficient values for all the suggested polynomials are listed in Tables 3 to 6.

Table 3. Factor values of the mathematical models for contraction length of 0.74m.

Profile	Factors					
	a	b	c	d	e	f
6 th	-13.3977652	23.79443099	-11.00492433	0.00	---	---
7 th	29 e-14	-13.3977652	23.79443099	-11.00492433	---	---
8 th	142.720289	-386.241879	375.137425	-148.054237	17.118771	---
10 th	-1407.3951	4975.92359	-6936.206053	4725.42799	-1547.441	187.381144

Table 4. Factors values of the mathematical model for the 9th-order profile with a length of 0.74 m.

Inflection point	9th – Order Polynomial Factors					
	a	b	c	d	e	f
0.5 L	-231.43830	770.689561	-977.67475	562.70613	-124.9207	---
0.55 L	-62.550893	270.782818	-422.778273	288.9572062	-74.27721	---
0.6 L	89.0147333	-177.8514372	75.2057506	43.2850875	-28.8278683	---
0.65 L	322.255870	-868.245202	841.542829	-334.774538	41.113162	---

Table 5. Factor values of the mathematical models for contraction length of 0.93m.

Profile	Factors					
	a	b	c	d	e	f
6 th	-3.40036071	7.5896051	-4.411457	7 e-15	---	---
7 th	-4 e-14	-3.40036071	7.5896051	-4.411457	---	---
8 th	22.933792	-78.0011059	95.21009989	-47.224209	6.8622679	---
10 th	-143.18705	636.2278	-1114.58233	954.29478	-392.7416	59.76814

Table 6. Factors values of the mathematical model for the 9th-order profile with a length of 0.93 m.

Inflection point	9th – order polynomial factors					
	a	b	c	d	e	f
0.5 L	-29.59199	123.84248	-197.44029	142.815149	-39.845426	---
0.55 L	-7.99783536	43.5122232	-85.3795888	73.3375093	-23.6918753	---
0.6 L	11.38153493	-28.579034228	15.18771533	10.9857807	-9.195098494	---
0.65 L	41.204037	-139.518745	169.948612	-84.965975	13.1136847	---

A preliminary investigation is conducting to ensure that it conforms to the required form within this work field, which should be a smooth concave-convex shape and starts immediately contracting from its beginning. This investigation shows that the 8th and 10th order are not compatible with the required shape, so they are omitted. The 7th order profile is also omitted because it gives the same profile as the 6th order profile. Table 7 shows the final form of the adopted polynomial with 0.74 m contraction length, and Figure 1 shows the profile shapes of these equations. Table 8 shows the adopted polynomials' final form with 0.93m contraction length, and Figure 2 shows the profile shapes.

Table 7. Adopted mathematical models for contractions of length 0.74m.

No.	E`quation
1	$h = \left[-10\left(\frac{x}{0.74}\right)^3 + 15\left(\frac{x}{0.74}\right)^4 - 6\left(\frac{x}{0.74}\right)^5 \right] (0.22) + 0.37$
2	$y = -13.397765x^6 + 23.794431x^5 - 11.004924x^4 + 0.37$
3	$y = -231.4383x^9 + 770.6895x^8 - 977.6747x^7 + 562.70613x^6 - 124.9207x^5 + 0.37$
4	$y = -62.55089x^9 + 270.782818x^8 - 422.77827x^7 + 288.957206x^6 - 74.27721x^5 + 0.73$
5	$y = 89.014733x^9 - 177.851437x^8 + 75.20575x^7 + 43.285087x^6 - 28.827868x^5 + 0.73$
6	$y = 322.25587x^9 - 868.2452x^8 + 841.54282x^7 - 334.77453x^6 + 41.11316x^5 + 0.73$

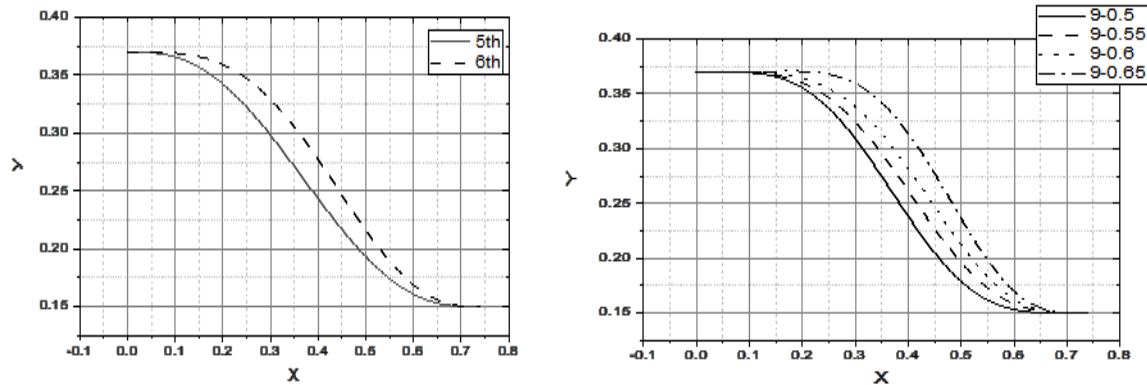


Figure 1. Contraction profile shapes for the 0.74m models.

Table 8. Adopted mathematical models for contractions of length 0.93m.

No.	equation
1	$h = \left[-10\left(\frac{x}{0.93}\right)^3 + 15\left(\frac{x}{0.93}\right)^4 - 6\left(\frac{x}{0.93}\right)^5 \right] (0.22) + 0.37$
2	$y = -3.40036x^6 + 7.589605x^5 - 4.411457x^4 + 0.37$
3	$y = -29.59199x^9 + 123.84248x^8 - 197.44029x^7 + 142.815149x^6 - 39.845426x^5 + 0.37$
4	$y = -7.99783536x^9 + 43.5122232x^8 - 85.3795888x^7 + 73.3375093x^6 - 23.6918753x^5 + 0.73$
5	$y = 11.381534x^9 - 28.579034x^8 + 15.1877153x^7 + 10.98578x^6 - 9.19509849x^5 + 0.73$
6	$y = 41.204037x^9 - 139.518745x^8 + 169.948612x^7 - 84.965975x^6 + 13.113684x^5 + 0.73$

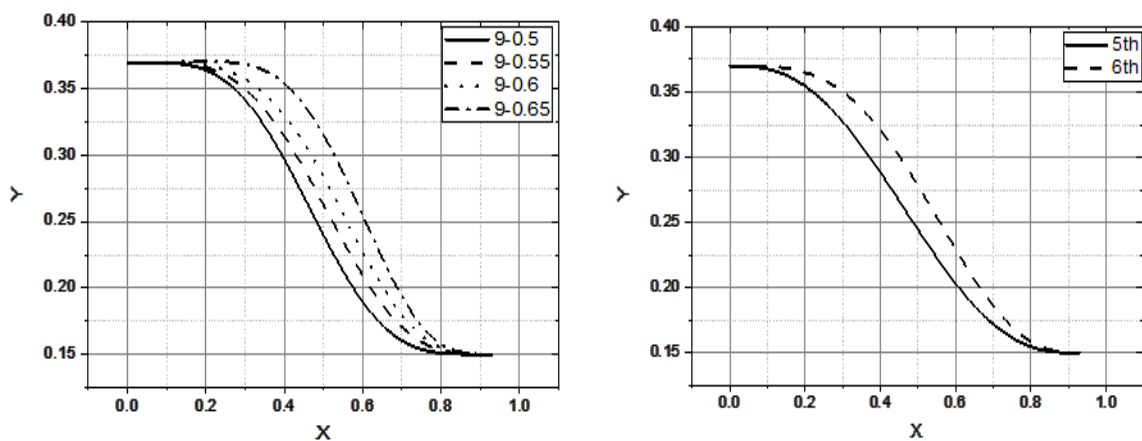


Figure 2. contraction profile shapes for the 0.93m models.

3. Contractions modeling and numerical analysis

The adopted twelve profile was modeled by SOLIDWORKS 19, as shown in Figure 3. These models are then simulated by using ANSYS FLUENT R19.0. Airflow in this work is assumed to be adiabatic, steady-state, incompressible, and turbulent flow. The investigation consisted of a series of three-dimensional Reynold-Average Navier-Stokes equations (RANS). Since the model is symmetric about the X and Y axis, a quarter of the model was simulated.

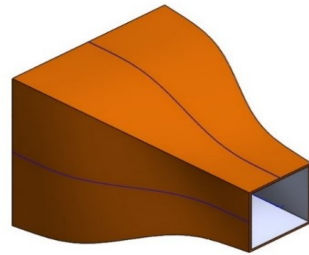


Figure 3. Contraction section model.

4. Mesh generation

The meshing method was multi-zone with mapped mesh type hexahedral elements and a structured approach. The grid's density was increased near the wall by adding (10-15) maximum inflation layer and the growth rate (1.2). The height of the first cell center adjacent to the wall is designed to provide a value of $(y^+ < 1)$ to overcome the need for wall function. On the other hand, the turbulence model needs higher y^+ values to guarantee that the solution includes the viscous sublayer for high accurate simulation. This simulation's element size is about $(7.5e-3)$; this size is slightly different among the models because of the change in profile shape. The quality of the mesh is high, smoothing with skewness mesh metric type with max. Moreover, the average skewness of (0.6) and (0.15), respectively, these numbers are also slightly different according to the model geometry. Figure 4 shows a sample of the final meshing result for the computational domain.

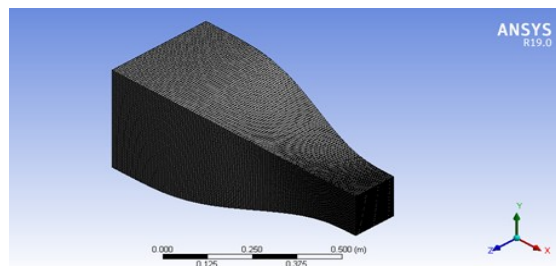


Figure 4. Sample of models meshing.

5. Mesh independence study

The simulation results cannot be trusted unless it is confirmed that the changes that occur to the flow characteristics are due to the change of conditions and not related to the number and type of grid cells (mesh independence). A unique study was performed to achieve grid viability by determining the appropriate number of reticulocytes needed for an accurate analysis. The study included a follow-up of the changes occurring to some flow characteristics until these values become stable or the percentage of change is tiny. This procedure required six simulations for each model, with a total of seventy-two simulations, to determine the appropriate mesh for each model separately. Table 9 shows a model to study the grid validity of one of the models.

Table 9. Mesh independence study for the 9th order contraction of length 0.93m.

Element size (m)	Number of elements	Exit velocity	Turbulent intensity	Exit total press
0.02	46550	1.995108	7.950808	2.3843
0.015	92125	1.995958	7.900831	2.3819
0.011	198016	1.996644	7.878365	2.3803
0.0095	282555	1.9969	7.873903	2.3799
0.007	629057	1.997412	7.873485	2.3794
0.005	1531504	1.997822	7.875362	2.3789

6. CFD model settings

The domain zones were two symmetric plans, exit, inlet, two walls, and air domain. The pressure-based with absolute velocity formulation is selected as the solver type. The turbulence model was the Menter's shear stress transportation model (K- ω SST) with double precision. The important feature of the (K- ω SST) model is that it combines the standard (K- ϵ) model in the free stream region and Wilcox (K- ω) model for the regions near the walls. This combination is capable of predicting the flow robustly in the free stream and near walls accurately. Besides, a study by Bouriga et al. [22] shows that Menter's turbulent model is proper to be used for nozzles investigations. The adopted solution method was pressure-velocity coupling with the Semi-Implicit Method for pressure Linked Equation (SIMPLE) algorithm to produce separate equations for pressure and velocity. The remarkable discretization gradient is based on the last squares cell. The rest of the equations were discretized with the second order-up wind (i.e., pressure, momentum, turbulent kinetic energy, and specific dissipation rate). The computation started with standard initialization from the inlet. The under relaxation factors have been modified to 0.3 for pressure, 0.5 for momentum, and 0.6 for turbulent kinetic energy and specific dissipation rate. The solution is assumed to be sufficiently converged for this simulation when the velocity, pressure, and turbulence residuals reach (1×10^{-6}). The simulation boundary conditions setup was velocity for inlet, pressure for the outlet, two stationary walls with the no-slip condition, and standard roughness value of (0.5), two symmetry plans. A mesh independence study has been done for each model to select the optimum number of cells required.

7. Numerical results and discussion

The numerical analysis includes simulating each model with three different velocities (i.e., 2, 7, and 10 m/s). The flow uniformity calculations are based on the velocity distribution at the exit plane, as shown in Figure 5. Due to the limited space and many results, one example will be shown for illustration, as shown in Table 10, representing the flow distribution at the exit plane of the 5th–order contraction and the boundary layer thickness. Table 11 shows the exact simulation results for contractions with 0.74m length at 2 m/s and presented graphically, as shown in Figure 6, to compare the contractions behavior—the same procedure done with all profiles with the three velocities. The final results refer to that the 9th-order profile with an inflection point at 0.65L is the one that can deliver the highest uniform flow comparing to the other models.

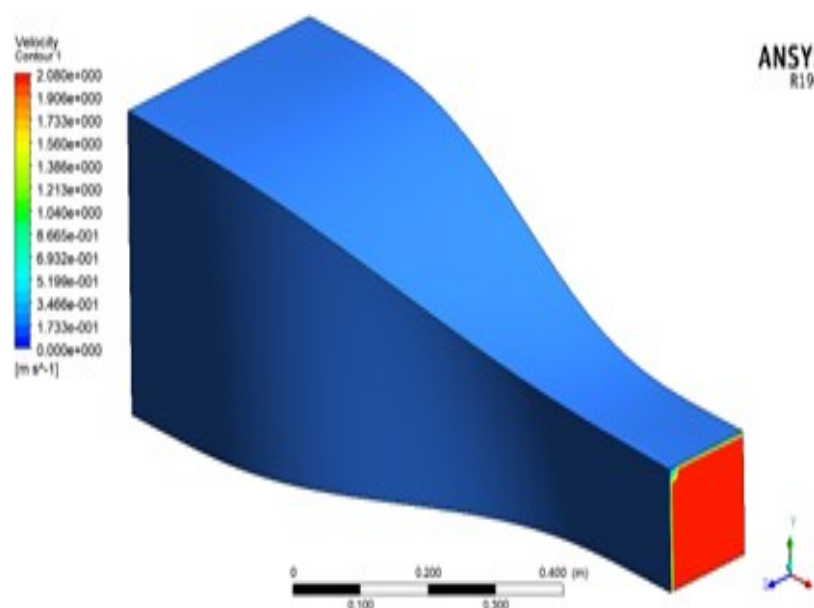


Figure 5. Velocity distribution for the 9th order profile at 2m/s.

Table 10. Velocity distribution at the exit plane.

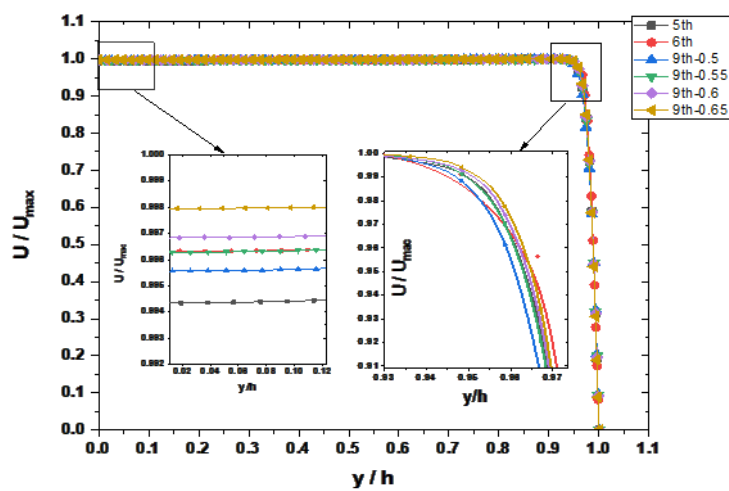
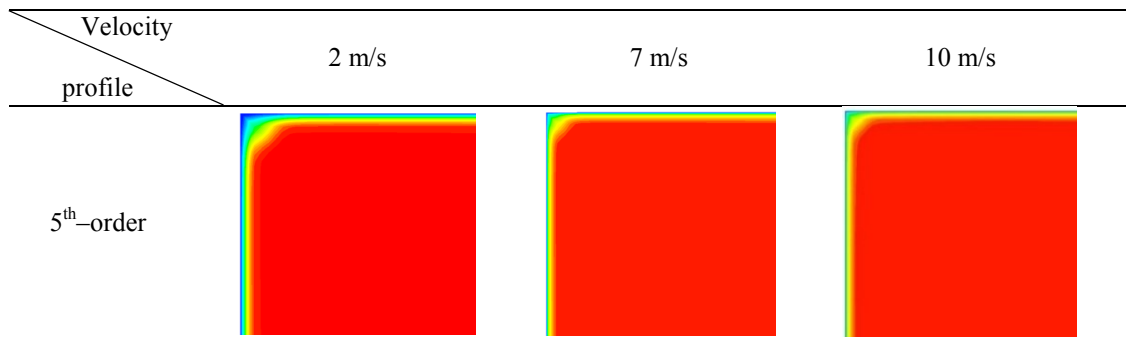


Figure 6. Uniformity profiles.

Table 11. Average uniformity and boundary layer thickness at 2 m/s for 0.74 m length models.

No.	Profile	δ (mm)	Average (U / U_{max})
1	5 th – order	10.65	0.996
2	6 th – order	10.5	0.998
3	9 th – order – 0.5	9.75	0.997
4	9 th – order – 0.55	9.7 5	0.998
5	9 th – order – 0.6	10.5	0.998
6	9 th – order – 0.65	9.6	0.999

The turbulent intensity was also investigated at the exit plane of the contractions. The intensity is measured according to the relation shown in Equation 5, where K is the turbulent kinetic energy resulting from the numerical analysis, and U is the exit velocity, as shown in Figure 7.

$$I = \sqrt{\frac{2K}{3U^2}} \tag{5}$$

Table 12 shows a sample of the simulation results and is graphically represented in Figure 8. The results also show that the 9th-order with an inflection point at the 0.65L is more stable than the other models, significantly increasing the velocity. Finally, as shown in Figure 9, the skin friction coefficient is simulated, which shows no zero regions at the contractions surfaces for all the suggested models, which means there is no boundary layer separation for all models. The results show low values at the contractions' concave parts, as shown in Figure 10.

According to these results, the 9th-order with an inflection point at 0.65L and length 0.93m shows a good performance comparing with the other profiles, so it was chosen to be manufacturing and experimentally testing.

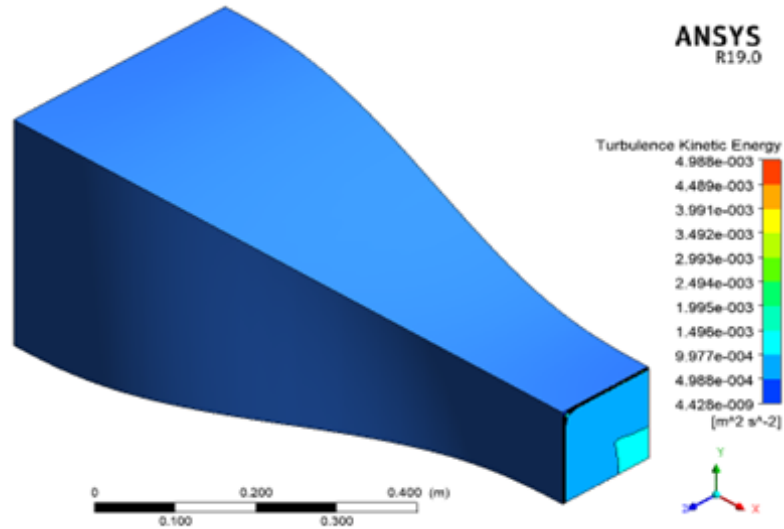


Figure 7. Exit plain turbulent kinetic energy.

Table 12. Turbulent intensity for the 0.93m contractions.

No.	profile	Turbulent intensity (I %)			$\Delta I\%$
		2 m/s	7 m/s	10 m/s	
1	5 th	0.238	0.267	0.304	21.7
2	6 th	0.234	0.25	0.261	10.3
3	9 th -0.5	0.238	0.307	0.337	29.4
4	9 th 0.55	0.234	0.262	0.289	19
5	9 th -0.6	0.234	0.259	0.275	14.9
6	9 th -0.65	0.234	0.262	0.267	12.4

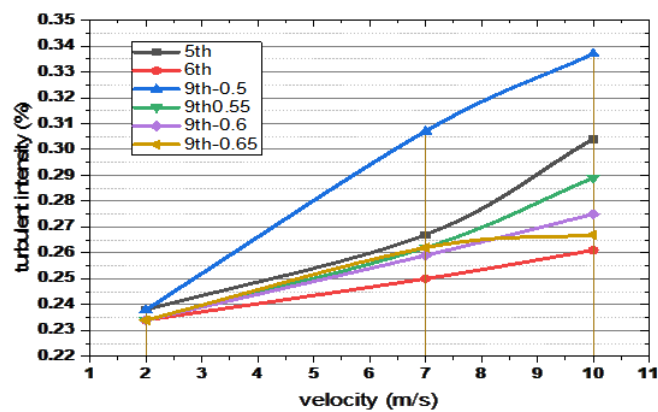


Figure 8. Turbulent intensity behavior with increasing velocity for the 0.93m contraction models.

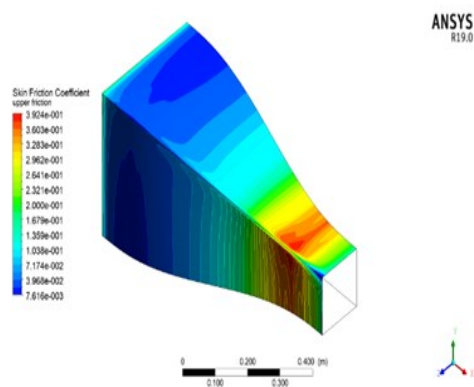


Figure 9. Skin friction coefficient counter.

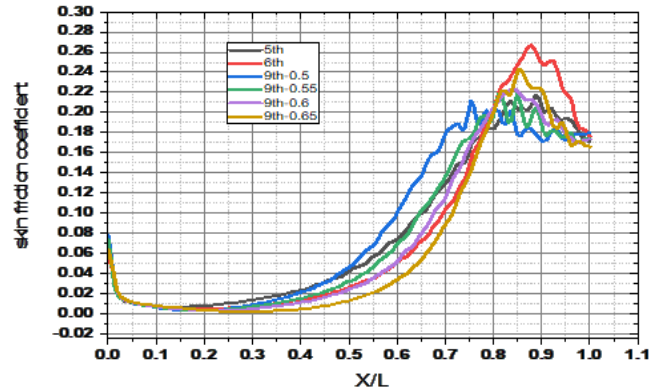


Figure 10. Skin friction coefficient for the 0.74m contraction models at 10 m/s.

8. Experimental work

To accurately shape the selected profile, a wooden model was made for the selected contraction section, as shown in Figure 11, to form a fiberglass contraction model. The used Fiberglass was the heavy type (450 g/m²). The resulting model is shown in Figure 12. The model was then cleaned and sanded.



Figure 11. Wooden model for the selected contraction section.



Figure 12. The fiberglass model for the selected contraction section.

To validate the performance of the new contraction section. A half-scale of the original smoke tunnel has been built, as shown in Figure 13, to experimentally show the new contraction influence on the visualization clarity of the streamlines in the test section for the aimed smoke tunnel. This tunnel includes an entrance, settling chamber with honeycomb and screen, test section, diffuser, and fan. The tunnel, also equipped with a control panel, contains two regulators to control the fan speed and voltage sensors to monitor the test speed stability after removing the anemometer. A digital anemometer type (GM8901+), as shown in Figure 14, is used to calibrate the test section's velocity. The calibration process is achieved by measuring the velocity at the test section and fix the fan speed at the required velocity, then removing the anemometer and starting the experiment by releasing the smoke. A simple smoke generator is built, as shown in Figure 15, to realize the visualization process. The device contains an electric heater, and the heating wires were wrapped with cotton, then the cotton was wetted with glycerin diluted with thirty percent water. A rake with 13 smoke tube mounted to the smoke generator to inject the smoke into the flow. The experimental results showed a significant improvement in the visualization process, as shown in Figure 16-17 comparing to the original model shown in Figure 18.

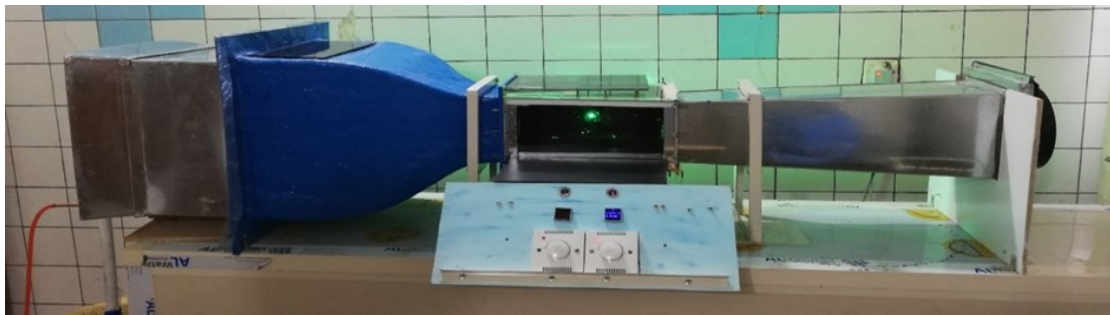


Figure 13. The final form of the combined smoke tunnel.



Figure 14. Smoke tunnel calibration with an anemometer.



Figure 15. Smoke generator.

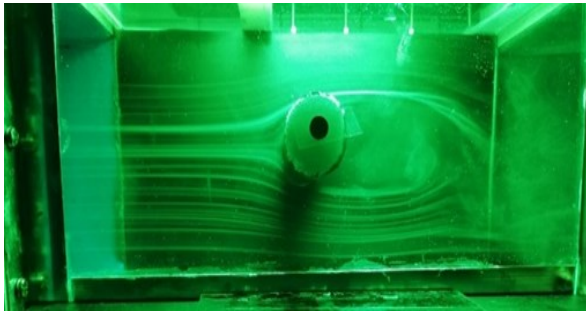


Figure 16. Cylinder test with 2.5 m/s.

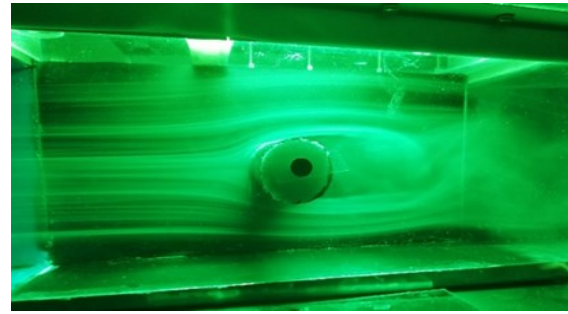


Figure 17. Cylinder test with 2 m/s.

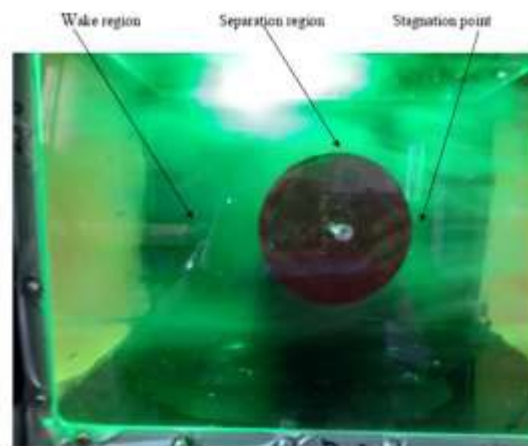


Figure 18. The old smoke tunnel visualization process with 2 m/s.

9. Conclusion

This work aims to improve the smoke tunnel that already exists in the Al-Nahrain university / mechanical engineering department laboratory by modifying the contraction section. New profiles are generated using polynomials of (6th, 7th, 8th, 9th, and 10th) order are suggested to be numerically investigated. Special care is taken with the 9th order profile by reforming it with a different inflection point (0.5L, 0.55L, 0.6L, and 0.65L). The numerical results showed an advantage to the 9th-order profile with an inflection point at 0.65L, so it has been chosen to be experimentally testing. The experimental work, including building a rig as a half-scale down copy of the original smoke tunnel. The contraction section of this rig was the new suggested one. The final visualization result shows a significant improvement in tunnel performance. This work also explains the direct influence of the contraction wall shape and length on the selected profiles' wind tunnel flow.

10. References

- [1] R D Mehta and P Bradshaw November 1979 *Design Rules for Small Low-Speed Wind Tunnels* (Aeronautical Journal) pp 718
- [2] James H Bell and Rabindra D Mehta 1988 *Contraction Design for Small Low-Speed Wind Tunnels* (JIAA TR- 84)
- [3] Yao-xi Su 1991 *Flow Analysis and Design of Three-Dimensional Wind Tunnel Contractions* (AIAA JOURNAL) vol 29
- [4] F-M Fang, J C Chen and Y T Hong 2001 *Experimental and Analytical Evaluation of Flow In A Square-To-Square Wind Tunnel Contraction* (Journal of Wind Engineering and Industrial Aerodynamics) vol 89
- [5] F Fang 1997 *A Design Method for Contractions with Square End Sections* (ASME J. Fluids

- Eng.) vol 119
- [6] Sargison J E Walker G J and Rossi R 2004 *Design and Calibration of a Wind Tunnel with a Two Dimensional Contraction* (Proceedings of the 15th Australasian Fluid Mechanics Conference)
- [7] D Brassard and M Ferchichi 2005 *Transformation of A Polynomial for A Contraction Wall Profile* (Journal of Fluids Engineering) vol 127
- [8] Mathew, J, Bahr, C, Carroll, B Sheplak, M and Cattafesta, L 2006 *Design, Fabrication, and Characterization of an Anechoic Wind Tunnel Facility* (11th AIAI/CEAS Aeroacoustics conference) pp 3052
- [9] C J Doolan 2007 *Numerical Evaluation of Contemporary Low-Speed Wind Tunnel Contraction Designs* (J. Fluids Eng. Trans. ASME) vol 129
- [10] Lindgren and Johansson 2002 *Design and Evaluation of a Low-Speed Wind-Tunnel with Expanding Corners* (Royal Institute of Technology Department of Mechanics Sweden Technical Report)
- [11] Sargison, J E, Walker, G J, and Rossi, R 2004 *Design and Calibration of a Wind Tunnel with a Two Dimensional Contraction* *Proceedings of the 15th Australasian Fluid Mechanics Conference*
- [12] Dehghan Manshadi M, Mirzaei M, Soltani M R and Ghorbanian K 2008 *Control of Pressure Gradient in the Contraction of a Wind Tunnel* (Int. J. Mech. Aerospace, Ind. Mechatron. Manuf. Eng.) vol 2
- [13] María Rodríguez Lastra, Jesús Manuel FernándezOro, MónicaGaldoVega, Eduardo Blanco Marigorta and Carlos Santolaria Morros Novel 2013 *Design and Experimental Validation of Contraction Nozzle for Aerodynamic Measurements in a Subsonic Wind Tunnel* (Journal of Wind Engineering and Industrial Aerodynamics) vol 118
- [14] A S Abdelhamed, Y El-S Yassen and M M El-Sakka 2014 *Design Optimization of Three Dimensional Geometry of Wind Tunnel Contraction* *Ain Shams Engineering Journal* vol 6
- [15] L Leifsson and S Koziel 2015 *Simulation-Driven Design of Low-Speed Wind Tunnel Contraction* (J. Comput. Sci.) vol 7
- [16] H Hoghooghi, M N Ahmadabadi and M D Manshadi 2016 *Optimization of a Subsonic Wind Tunnel Nozzle with Low Contraction Ratio via Ball-spine Inverse Design Method* (J. Mech. Sci. Technol.) vol 30
- [17] Y H Kao, Z W Jiang, and S C Fang 2017 *A Computational Simulation Study of Fluid Mechanics of Low-Speed Wind Tunnel Contractions* (Fluids) vol 2
- [18] Lakishmar R and Ranjan Basak 2017 *Analysis of Transformed Sixth Order Polynomial Curve for The Contraction of Wind Tunnel by Using OpenFOAM* (Seventh International Conference on Theoretical, Applied, Computational and Experimental Mechanics)
- [19] E S Zanoun 2018 *Flow Characteristics in Low-Speed Wind Tunnel Contractions: Simulation and Testing* (Alexandria Eng. J) vol 57
- [20] T Morel 1976 *Design of Two-dimensional Wind Tunnel Contractions* (ASME J. Fluids Eng.) vol 99 pp 371-377
- [21] R Lakshman and R Basak 2018 *Analysis of Transformed Fifth-order Polynomial Curve for the Contraction of a Wind Tunnel by Using OpenFOAM* (IOP Conference Series: Materials Science and Engineering) vol 377
- [22] Bouriga, M Lemyre-Baron, J Morency and F Weiss, J 2014 *Preliminary Experimental And Numerical Investigations of The Flow In The Contraction of A Boundary Layer Wind Tunnel* *Trans. Can. Soc. Mech. Eng.* vol 38